edge in the 2D real space of a cylindrical geometry. From the viewpoint of the 1D chain, the band structure implies that two electrons per spin are pumped from the right edge to the left by the cyclic evolution, and the charge pumping is topologically protected. For the reverse evolution by transporting left-chiral solitons, the edge currents in the 2D system flow in the opposite direction, and so does the charge pumping in the 1D chain. In contrast, for the nonchiral evolution of AA → BB → AA, which do not encircle the origin in the phase space, the edge states are not chiral, and there is no charge pumping (*26*).

The quantized charge pumping by chiral solitons can be understood physically by considering electric polarization. Figure 3C depicts the center of the bonding charges, called the Wannier center (*28*), for the four ground phases. For the right-chiral evolution of AA → BA, the charge center moves to the left, resulting in the increase of electric polarization by $|e|$ (*26*). Thus, it produces charge pumping of one electron from the right edge to the left. For the nonchiral evolution of AA → BB, the charge center moves by half of the unit cell, and the bonding charges split into both the left and right directions, producing no change in polarization and no charge pumping.

For a 1D system to have a chiral soliton, it should have more than two degenerate ground phases, and a set of its solitons should form a topologically nontrivial closed path in the phase space. Solitons in systems with two degenerate ground phases (*8*, *14*) are not chiral, regardless of whether the sublattice symmetry is broken or not (*29*), and thus for those systems charge pumping is not possible unless there are external time-varying potentials (*23*, *24*, *30*). In our system with four ground phases, charge pumping is allowed by transporting chiral solitons. The pumping of four electrons by one-cycle evolution is topologically protected—i.e., secure from defects or perturbations that do not close the band gap. Furthermore, because of the C_4 symmetry among the ground phases, each soliton delivers just one charge across the chain. This property can be exploited for future information storage devices where each bit of information is written by a single electron (*31*).

Our work suggests further studies of the 1D counterparts of other interesting topological systems in higher dimensions, such as the 1D realization of the quantum spin Hall system.

REFERENCES AND NOTES

1. M. Z. Hasan, C. L. Kane, *Rev. Mod. Phys.* **82**, 3045–3067 (2010).
2. X.-L. Qi, S.-C. Zhang, *Rev. Mod. Phys.* **83**, 1057–1110 (2011).
3. B. I. Halperin, *Phys. Rev. B* **25**, 2185–2190 (1982).
4. F. D. M. Haldane, *Phys. Rev. Lett.* **61**, 2015–2018 (1988).
5. D. J. Thouless, M. Kohmoto, M. P. Nightingale, M. den Nijs, *Phys. Rev. Lett.* **49**, 405–408 (1982).
6. C. L. Kane, E. J. Mele, *Phys. Rev. Lett.* **95**, 226801 (2005).
7. L. Fu, C. L. Kane, E. J. Mele, *Phys. Rev. Lett.* **98**, 106803 (2007).
8. W. P. Su, J. R. Schrieffer, A. J. Heeger, *Phys. Rev. Lett.* **42**, 1698–1701 (1979).
9. C. L. Kane, *Topological Insulators*, M. Franz, L. Molenkamp, Eds. (Elsevier, Oxford, 2013), pp. 3–34.
10. R. Jackiw, C. Rebbi, *Phys. Rev. D Part. Fields* **13**, 3398–3409 (1976).
11. The chiral domain walls in 1D quantum spin chains were also called chiral solitons (*12*), but they are disparate from the topological edge states of this work.
12. H.-B. Braun *et al.*, *Nat. Phys.* **1**, 159–163 (2005).
13. S. A. Brazovski, *Sov. Phys. JETP* **51**, 342–253 (1980).
14. M. J. Rice, E. J. Mele, *Phys. Rev. Lett.* **49**, 1455–1459 (1982).
15. R. Jackiw, G. Semenoff, *Phys. Rev. Lett.* **50**, 439–442 (1983).
16. J. Goldstone, F. Wilczek, *Phys. Rev. Lett.* **47**, 986–989 (1981).
17. S. Kivelson, *Phys. Rev. B* **28**, 2653–2658 (1983).
18. H. W. Yeom *et al.*, *Phys. Rev. Lett.* **82**, 4898–4901 (1999).
19. O. Bunk *et al.*, *Phys. Rev. B* **59**, 12228–12231 (1999).
20. C. González, J. Ortega, F. Flores, *New J. Phys.* **7**, 100 (2005).
21. T.-H. Kim, H. W. Yeom, *Phys. Rev. Lett.* **109**, 246802 (2012).
22. J. R. Ahn *et al.*, *Phys. Rev. Lett.* **93**, 106401 (2004).
23. D. J. Thouless, *Phys. Rev. B* **27**, 6083–6087 (1983).
24. Q. Niu, D. J. Thouless, *J. Phys. A* **17**, 2453–2462 (1984).
25. X.-L. Qi, T. L. Hughes, S.-C. Zhang, *Phys. Rev. B* **78**, 195424 (2008).
26. Materials and methods are available as supplementary materials on *Science* Online.
27. R. F. Peierls, *Quantum Theory of Solids* (Clarendon, Oxford, 1955).
28. N. Marzari, A. A. Mostofi, J. R. Yates, I. Souza, D. Vanderbilt, *Rev. Mod. Phys.* **84**, 1419–1475 (2012).
29. The chiral symmetry of 1D Peierls systems is the sublattice symmetry (*9*). The chiral symmetry breaking is a necessary, but not sufficient, condition for the chiral soliton (*26*).
30. D. Xiao, M.-C. Chang, Q. Niu, *Rev. Mod. Phys.* **82**, 1959–2007 (2010).
31. There are interwire interactions in the present In/Si(111) system (*21*). They do not modify the topological structure and edge states of a single wire, but they force solitons to aggregate into a domain wall perpendicular to the wire and need to be avoided for the single-wire manipulation.

ACKNOWLEDGMENTS

This work was supported by the Institute for Basic Science (IBS-R014-D1). We thank K. S. Kim and H. W. Lee for discussions. H.W.Y. appreciates the initial work of S. Takeda and D. M. Oh in shaping the soliton idea in In/Si(111).

SUPPLEMENTARY MATERIALS

www.sciencemag.org/content/350/6257/182/suppl/DC1
Materials and Methods
Supplementary Text
Figs. S1 to S9
References (*32*–*36*)

18 January 2015; accepted 27 August 2015
10.1126/science.aaa7055

SURFACE CHEMISTRY

Finding optimal surface sites on heterogeneous catalysts by counting nearest neighbors

Federico Calle-Vallejo,[1,2]*† Jakub Tymoczko,[3,4]* Viktor Colic,[3,5] Quang Huy Vu,[6] Marcus D. Pohl,[5] Karina Morgenstern,[6] David Loffreda,[1] Philippe Sautet,[1]† Wolfgang Schuhmann,[3,4] Aliaksandr S. Bandarenka[3,5,7]†

A good heterogeneous catalyst for a given chemical reaction very often has only one specific type of surface site that is catalytically active. Widespread methodologies such as Sabatier-type activity plots determine optimal adsorption energies to maximize catalytic activity, but these are difficult to use as guidelines to devise new catalysts. We introduce "coordination-activity plots" that predict the geometric structure of optimal active sites. The method is illustrated on the oxygen reduction reaction catalyzed by platinum. Sites with the same number of first-nearest neighbors as (111) terraces but with an increased number of second-nearest neighbors are predicted to have superior catalytic activity. We used this rationale to create highly active sites on platinum (111), without alloying and using three different affordable experimental methods.

Slight changes in the surface structure of catalytic materials can have large impacts on the products and energetics of chemical reactions (*1*, *2*). However, not all sites at catalytic surfaces have the same activity or selectivity, which gives rise to the concept of structure sensitivity (*3*–*5*). Generally, identification of active sites is a challenging task that requires the combination of several approaches (*6*, *7*). A rational way of designing catalysts should first identify the optimal active sites and then engineer surfaces where the presence of such sites is maximized. Modern computational screening techniques can provide the atomic-scale insight needed to elaborate simple catalyst design rules (*2*, *8*). Such rules are the starting point to engineer target active sites on catalytic surfaces (*9*–*12*). The connection between these two steps must be straightforward and clear, which is not trivial in practice. The difficulties originate from an important detail: Existing computational techniques outline optimal energetic properties, which can be met by countless materials. Therefore, it is desirable to create procedures that generate more precise design rules.

Consider the specific case of the oxygen reduction reaction (ORR), $O_2 + 4(H^+ + e^-) \rightarrow 2H_2O$, a

[1]Université de Lyon, CNRS, École Normale Supérieure de Lyon, Université Claude Bernard Lyon 1, Laboratoire de Chimie, 46 Allée d'Italie, 69364 Lyon Cedex-07, France. [2]Leiden Institute of Chemistry, Leiden University, Post Office Box 9502, 2300 RA Leiden, Netherlands. [3]Center for Electrochemical Sciences, Ruhr-Universität Bochum, Universitätstrasse 150, 44780 Bochum, Germany. [4]Analytical Chemistry, Ruhr-Universität Bochum, Universitätstrasse 150, 44780 Bochum, Germany. [5]Energy Conversion and Storage, Physik-Department, Technische Universität München, James-Franck-Straße 1, 85748 Garching, Germany. [6]Physical Chemistry I, Ruhr-Universität Bochum, Universitätstrasse 150, 44780 Bochum, Germany. [7]Nanosystems Initiative Munich, Schellingstraße 4, 80799 Munich, Germany.
*These authors contributed equally to this work.
†Corresponding author. E-mail: bandarenka@ph.tum.de (A.S.B.); philippe.sautet@ens-lyon.fr (P.S.); f.calle.vallejo@chem.leidenuniv.nl (F.C.-V.)

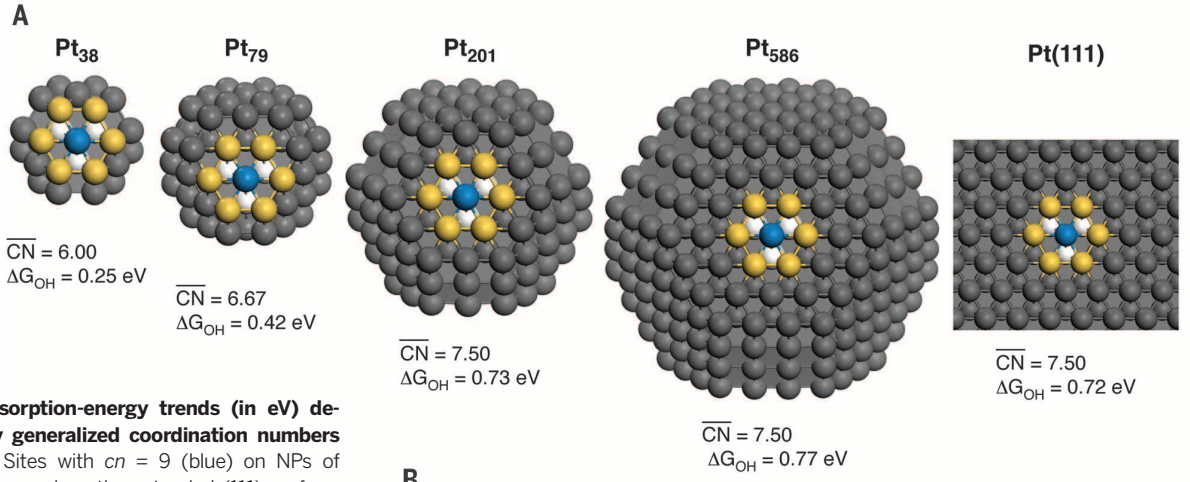

Fig. 1. Adsorption-energy trends (in eV) described by generalized coordination numbers ($\overline{CN}$). (**A**) Sites with *cn* = 9 (blue) on NPs of various sizes and on the extended (111) surface. The six surface nearest neighbors (yellow) and the three in the subsurface (white) are marked. Despite the identical coordination (*cn* = 9), ΔG_{OH} can differ by ~0.5 eV. The differences are due to the second-nearest neighbors. (**B**) Trends in ΔG_{OH} and ΔG_{OOH} described by $\overline{CN}$, including extended surfaces (brown) and truncated octahedron (●), cuboctahedron (■), and tetrahedron (▲) NPs: Pt_{586} (yellow), Pt_{201} (blue), Pt_{147} (gray), Pt_{79} (magenta), Pt_{68} (orange), and Pt_{38} (green). The reactions used to calculate the adsorption energies appear as insets. Least-squares fits are provided together with mean and maximum absolute errors (MAE and MAX).

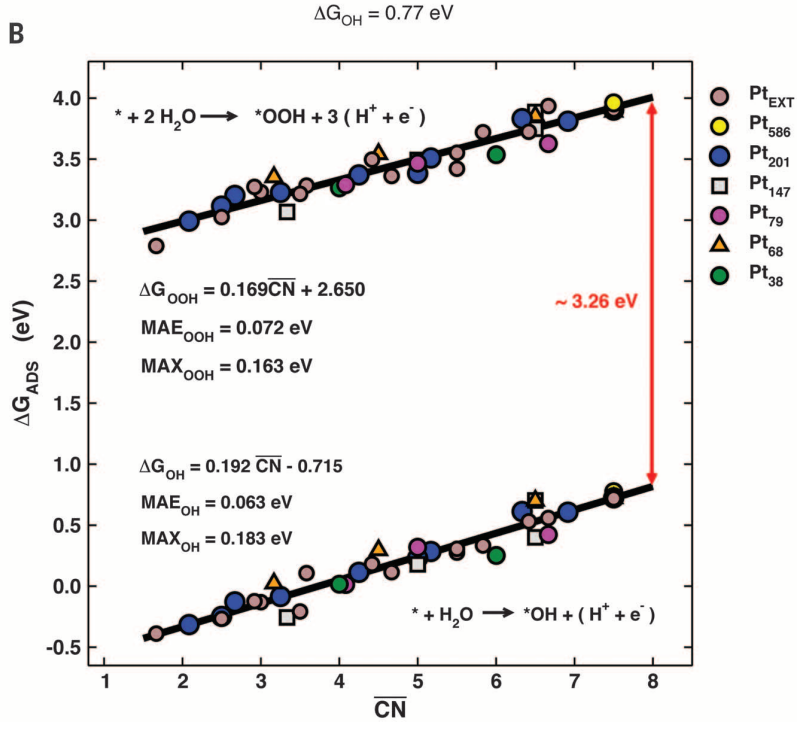

Fig. 2. Coordination-activity plot. (**A**) Potentials for the two limiting steps on extended surfaces and NPs. Points B and C (in light blue) are given for two cavities on Pt(111). The potential-determining step on the left (low coordination – strong binding) and right (high coordination – weak binding) sides of the volcano are indicated. Theoretical overpotentials (η_{ORR}) are the vertical difference between the points and the equilibrium potential (red dashed line). Optimal catalysts have $\overline{CN} \approx 8.3$ and *OH adsorption energies ~0.15 eV weaker than Pt(111) (area in gray). (**B**) Top view of a six-atom cavity on Pt(111) with $\overline{CN} = (6 \times 10 + 3 \times 12)/12 = 8.00$. (**C**) Five-atom cavity on Pt(111) with $\overline{CN} = (4 \times 10 + 2 \times 11 + 3 \times 12)/12 = 8.17$.

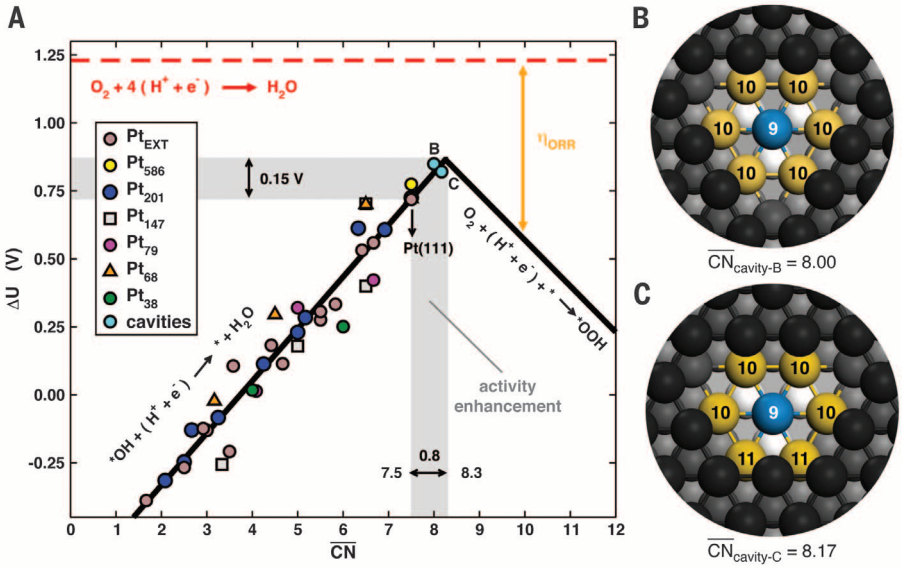

key reaction for proton exchange membrane fuel cells that is normally catalyzed by Pt, which is scarce and expensive. Although many challenges remain (*13*), rational catalyst design has opened new avenues for the ORR through volcano-type activity plots (*8*, *14*–*16*). These plots are based on the Sabatier principle, which states that good catalysts balance the strength of adsorption and desorption of key reaction intermediates. Volcano plots typically correlate surface adsorption energies with estimates of the catalytic activity of materials. By means of density functional theory (DFT) calculations, they predict that optimal ORR catalysts must bind hydroxyl species (*OH) ~0.1 eV (2.3 kcal/mol) more weakly than Pt(111) (*8*, *15*). Several studies have used this criterion to find alloy catalysts with high ORR activities (*8*, *12*, *15*, *17*). However, this condition can be met by numerous materials, including metals and alloys (*15*), oxides (*18*), functionalized graphitic materials, and porphyrins (*19*, *20*). Therefore, screening routines are used to select suitable candidates from large databases in which the composition, structure, and adsorption energies of materials are known beforehand. Creating such databases demands considerable time and computational expenses.

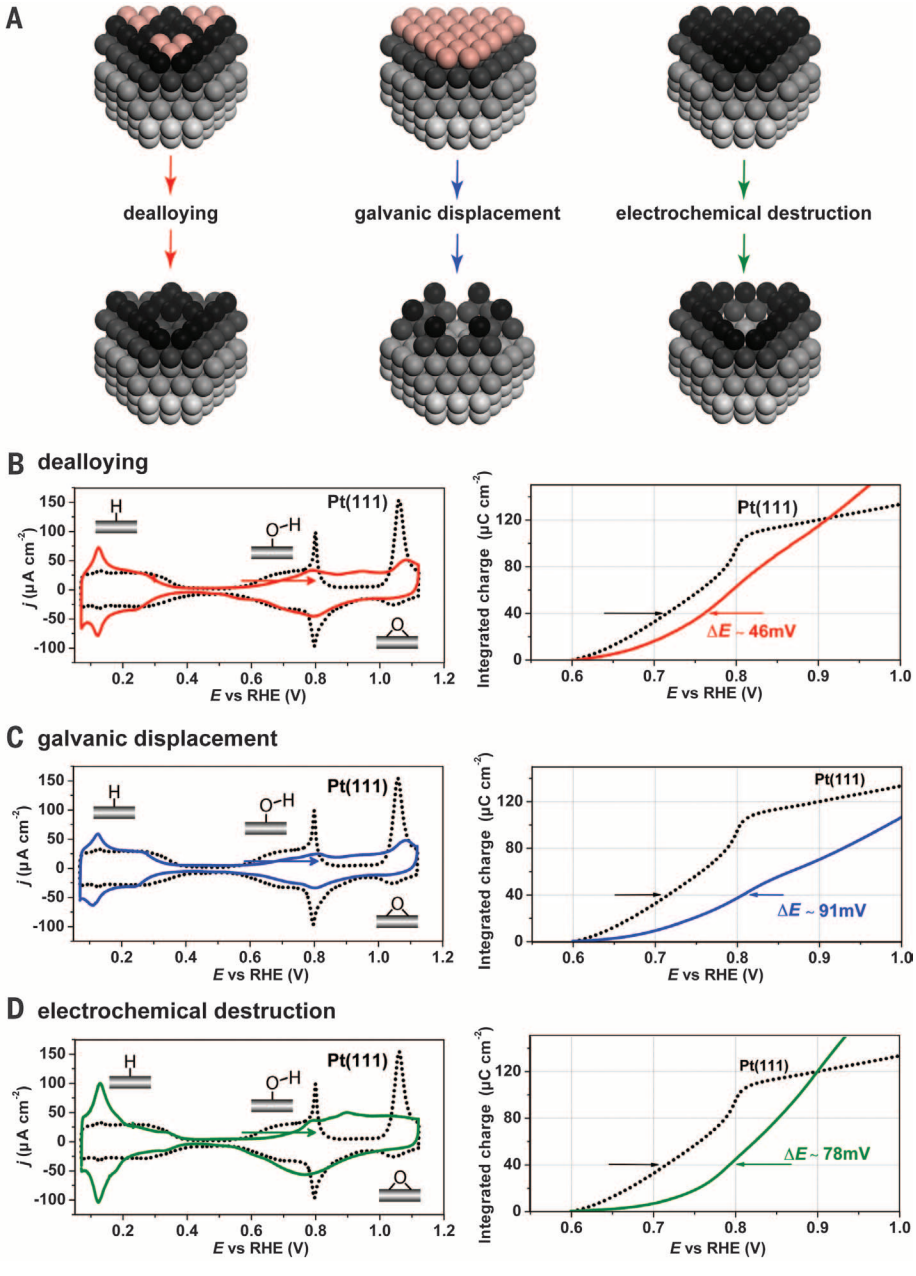

Fig. 3. Electrochemical experiments on pristine and defective Pt(111). (**A**) Schematics of the approaches used to create defects at Pt(111). Cu atoms appear in red and Pt atoms in gray or black, according to the depth with respect to the surface layer. (**B** to **D**) Left: cyclic voltammograms characterizing Pt(111) upon the following electrochemical modifications: (B) dealloying of a Cu/Pt(111) SA (red); (C) five galvanic displacements (blue); and (D) electrochemical destruction of Pt(111) (green). Right: integrated anodic parts of the corresponding voltammograms, scan rate dE/dt = 50 mV s^{-1}, Ar-saturated 0.1 M $HClO_4$. The positive shifts indicate weakened *OH adsorption energies and enhanced ORR activity compared to Pt(111).

We introduce here "coordination-activity plots," which outline the geometric structure of optimal active sites. The method is illustrated on the ORR, for which we devise Pt catalysts that are 3.5 times more active than Pt(111).

Usually, trends in adsorption energies for small species on extended surfaces of a given transition metal are well described by the coordination number (*cn*) of the surface sites (*21*, *22*). However, *cn* loses its accuracy when nanoparticles (NPs, the typical form of metals on high–surface area catalysts) are considered because of "finite-size effects" (*23*, *24*), so more sophisticated descriptors are needed (*25*). For example, in Fig. 1A, all sites in blue have nine nearest neighbors, that is *cn* = 9, but the adsorption energies of *OH calculated with DFT [see fig. S21 and tables S2 and S3 in the supplementary materials (*26*)] can differ by more than 0.5 eV (11.5 kcal/mol). A simple strategy to allow for direct comparison of NPs and extended surfaces is the use of "generalized" coordination numbers ($\overline{CN}$) (*27*), which introduce a weight to each first-nearest neighbor atom *j*, corresponding to its own coordination number [*cn*(*j*)] The formula used to estimate $\overline{CN}$ for a site *i* is (*27*)

$$\overline{CN}(i) = \sum_{j=1}^{n_i} \frac{cn(j)}{cn_{max}} \quad (1)$$

The sum includes all of the first-nearest neighbors, and the division by the maximum number of first-nearest neighbors in the bulk (cn_{max}) ensures that $\overline{CN}$ spans the range between 0 and 12 in face-centered cubic metals, similarly to conventional *cn*. For instance, the blue site on Pt_{38} in Fig. 1A has six neighbors with *cn* = 6 (yellow) and three with *cn* = 12 (white), so $\overline{CN} = (6 \times 6 + 3 \times 12)/12 = 6.00$ [section S3.1 in (*26*) shows how to compute $\overline{CN}$ for all sites under study]. This simple extension explains the variations in Fig. 1A and results in the linear relation in Fig. 1B, where the trends in adsorption energies of *OH and *OOH, ΔG_{OH} and ΔG_{OOH}, on all sites on Pt NPs of various sizes (0.7 to 2.6 nm) and shapes (truncated octahedron, cuboctahedron, tetrahedron) and extended surfaces are presented; data are reported for terraces, edges, corners, steps, kinks, and metal adatoms [see tables S2 and S3 in (*26*)]. Figure S21 shows that $\overline{CN}$ describes adsorption-energy trends more accurately than *cn*. Additionally, because $\overline{CN}$ is arithmetical, its assessment does not require DFT calculations.

Following the ORR model in (*16*), the two potential-determining steps are [see Fig. 2 and section S1 in (*26*)] (i) the first proton-electron transfer, in which O_2 is transformed into *OOH; or (ii) the last proton-electron transfer, in which

*OH is transformed into H_2O. Thus, within this model, the ORR activity depends primarily on ΔG_{OOH} and $-\Delta G_{OH}$. An activity plot is formed when the reaction energies of steps (i) and (ii) are evaluated as a function of a given descriptor. If adsorption energies are used as descriptors, only the optimal adsorption properties will be identified (*2*, *15*, *16*). If structural parameters are used as descriptors, the outcome will be the geometry of optimal sites. The choice between energetic and geometric descriptors is determinant, as illustrated in Fig. 2A, where a coordination-activity plot is presented [see also fig. S1 in (*26*)]. This plot shows that optimal Pt surface sites for the ORR possess $\overline{CN} \approx 8.3$. In agreement with energetic volcano plots (*8*, *15*), ΔG_{OH} on optimal catalysts is ~0.15 eV weaker than on Pt(111). Besides, the additional structural prediction ($\overline{CN} \approx 8.3$) can be used to guide experiments.

First, note that $\overline{CN} = 7.50$ for (111) terraces in extended surfaces and sufficiently large NPs (Figs. 1 and 2). If the top of the volcano is found at $\overline{CN} \approx 8.3$, optimal catalytic sites must have more neighbors than (111) terraces. Sites with $cn = 10$ [e.g., bottom of (100) step sites] or $cn = 11$ [e.g., troughs of (110) facets or bottom of (111) step sites] have $\overline{CN}$ values between 8.75 and 9.50, which exceed the optimal value and are problematic because of steric hindrance, weak adsorption energies, and proximity to undercoordinated sites, resulting in adsorbate diffusion to neighboring sites.

If no more first-nearest neighbors can be added to Pt(111) sites, a way of producing sites with $\overline{CN} \approx 8.3$ is by changing the coordination numbers of such first-nearest neighbors—namely, the number of second-nearest neighbors of the active site. Figure 2, B and C, shows two one-layer-deep cavities on Pt(111), corresponding to the removal of six (B) and five (C) adjacent surface atoms. In the configuration in Fig. 2B, the atom in the middle of the cavity (blue) has $cn = 9$, but its six in-plane nearest neighbors (yellow) have $cn = 10$ [one more neighbor compared to Pt(111)] and its three subsurface neighbors (white) have $cn = 12$, so $\overline{CN}_B = (6 \times 10 + 3 \times 12)/12 = 8.00$. Similarly, the active site in Fig. 2C has $\overline{CN}_C = (4 \times 10 + 2 \times 11 + 3 \times 12)/12 = 8.17$. The overpotentials for these sites are lower than on Pt(111) by ~0.10 to 0.13 V. Several other configurations may exist, but the design rule is clear, general, and simple: Enhanced Pt(111) sites for the ORR must have an increased number of second-nearest neighbors, so that $cn > 9$ for the first-nearest neighbors of the active site. Such a conclusion could not be obtained using cn as descriptor in Fig. 2, as it does not account for second-nearest neighbors [see fig. S21 in (*26*)].

We used these theoretical guidelines to engineer active sites at Pt(111) with one of three approaches illustrated in Fig. 3A [see section S2 in (*26*)]: (i) We stripped away Cu atoms electrochemically from the top layer of an ordered Cu/Pt(111) surface alloy (SA) (*9*); (ii) we exchanged a deposited Cu-overlayer with Pt ions in solution via galvanic displacement (*28*) to form Pt "surface islands"; or (iii) we formed a subsurface Pt oxide, which we then reduced during a cathodic potential scan, causing desorption of some Pt atoms from the surface (*29*, *30*) to create both (desirable) small and (undesirable) large cavities. These approaches create surfaces with different adsorption energies of *OH compared to Pt(111), as shown in Fig. 3, B to D [see also figs. S3 to S5, S8, S10, and S16 to 19 in (*26*)].

For Pt-based ORR catalysts, the most insightful part of the cyclic voltammograms is the *OH adsorption-desorption region (0.6 to 1.0 V in Fig. 3, B to D). For the three modified electrodes, a noticeable weakening of the *OH adsorption is observed, as the two peaks at ~0.8 V appear at more positive potentials. The interaction between *OH and the surface is quantified in the right panels of Fig. 3, B to D. Sizable positive shifts are observed for dealloyed Cu/Pt(111) SA (~46 mV), and for Pt(111) electrodes after galvanic displacement (~91 mV) and electrochemical oxidation (~78 mV). Thus, these catalysts bind *OH more weakly than pristine Pt(111) (see figs. S6 to S11). Normally, the *OH adsorption potentials predicted from volcano plots compare well to experimental onset potentials for *OH adsorption (*15*, *17*). Here, the experimental shifts in the *OH adsorption peaks (~0.05 to 0.09 V) with respect to Pt(111) in Fig. 3 are also in agreement with those in Fig. 2A (0.10 to 0.13 V).

The activities of Pt(111), various (111) defective electrodes, and similarly treated polycrystalline Pt electrodes (Pt_{pc}) presented in Fig. 4 show that specific defects can increase the activity ~3.5 times compared to Pt(111). This increase in catalytic activity cannot be explained by the modest increase in the number of accessible surface adsorption sites [maximum 15%; see (*26*)]. However, defects do not enhance the ORR activity of all Pt electrodes. Figure 4A shows that defects on Pt_{pc} did not noticeably enhance the ORR activity [see also figs. S13 and S14 in (*26*)]. This is attributed to different corrosion mechanisms on Pt facets that lead to the formation of dissimilar defects (*31*).

Because only specific kinds of defects are beneficial, "template" methods generating uniform surfaces with abundant target defects are needed to enhance the ORR activity. This is important for the design of highly active NPs. Convex NPs (Fig. 1) have numerous undercoordinated sites that are not ORR active, and only (111) sites on sufficiently large NPs are similar to extended Pt(111) (see Fig. 2A). Thus, concave geometries are recommendable to introduce sites with $\overline{CN} \approx 8.3$ and enhance the ORR activity (*10*).

Figure 4B shows the ORR current densities of the most active defective surface in this work and those of state-of-the-art Pt-based catalysts. Pt(111) with cavities possesses ORR activities that exceed those of several active alloys. Therefore, the optimal electronic and coordination configuration of Pt ORR catalysts is close but not identical to that of (111) terraces, and alloying or adding second-nearest neighbors have similar beneficial effects.

Figure S22 in (*26*) shows the ORR coordination-activity plot for gold, where optimal sites correspond to (100) terraces or possess $\overline{CN} \approx 5.1$. In (*26*), we outline the extension of $\overline{CN}$ to alloys and other compounds. Coordination-activity plots could be used to model other catalytic reactions such as H_2O_2 production, CO_2/CO reduction, and nitrate reduction, as the relation between adsorption energies and surface coordination exists on metals such as Cu, Ag, and Au and for adsorbates such as *O, *O_2, *H_2O, *H_2O_2, *CO, *CH, *N, and *NO_3^- (*21*, *22*, *24*, *27*). Thus, this work opens up the path in heterogeneous catalysis for the design of optimal surface sites utilizing coordination rationales.

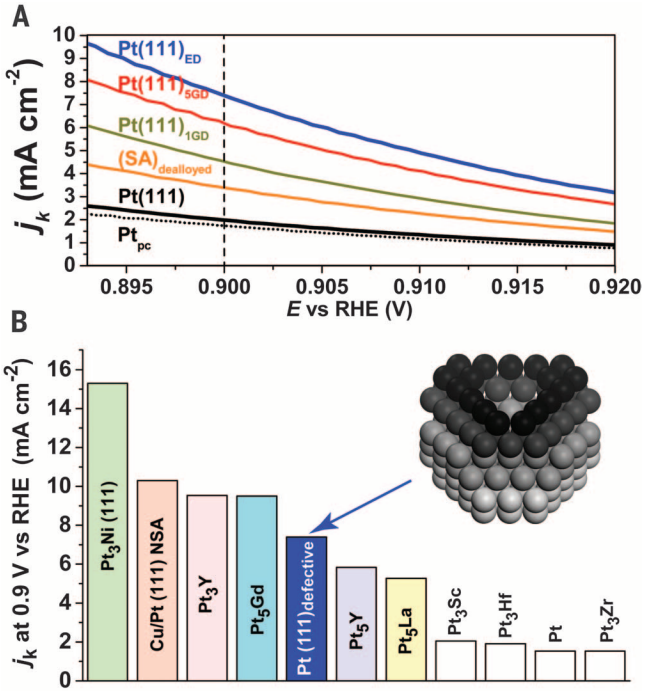

Fig. 4. Comparison between catalysts in this and in previous studies. (**A**) Kinetic current densities in O_2-saturated 0.1 M $HClO_4$ for defective Pt_{pc} (dotted line); Pt(111) (black); dealloyed Cu-Pt(111) SA, $(SA)_{dealloyed}$ (orange); Pt(111) electrodes modified via galvanic displacement, $Pt(111)_{1GD}$ (1 Cu monolayer displaced, green) and $Pt(111)_{5GD}$ (5 monolayers Cu displaced, red); and electrochemical destruction (10 cycles, blue), $Pt(111)_{ED}$. (**B**) ORR activities for defective $Pt(111)_{ED}$ and Pt_3Ni (*6*); Cu-Pt(111) near-surface alloy (*17*), Pt_3Y and Pt_3Sc (*8*), Pt_5Gd (*12*); Pt_5Y, Pt_3Zr, Pt_3Hf, and Pt_5La (*15*). The potential for comparison is 0.9 V.

REFERENCES AND NOTES

1. T. Zambelli, J. Wintterlin, J. Trost, G. Ertl, *Science* **273**, 1688–1690 (1996).
2. J. K. Nørskov, T. Bligaard, J. Rossmeisl, C. H. Christensen, *Nat. Chem.* **1**, 37–46 (2009).
3. R. A. Van Santen, *Acc. Chem. Res.* **42**, 57–66 (2009).
4. G. A. Somorjai, J. Carrazza, *Ind. Eng. Chem. Fundam.* **25**, 63–69 (1986).
5. I. Lee, F. Delbecq, R. Morales, M. A. Albiter, F. Zaera, *Nat. Mater.* **8**, 132–138 (2009).
6. V. R. Stamenkovic *et al*., *Science* **315**, 493–497 (2007).
7. M. Behrens *et al*., *Science* **336**, 893–897 (2012).
8. J. Greeley *et al*., *Nat. Chem.* **1**, 552–556 (2009).
9. A. S. Bandarenka *et al*., *Angew. Chem. Int. Ed.* **51**, 11845–11848 (2012).
10. L. Dubau *et al*., *J. Mater. Chem. A* **2**, 18497–18507 (2014).
11. P. Strasser *et al*., *Nat. Chem.* **2**, 454–460 (2010).
12. M. Escudero-Escribano *et al*., *J. Am. Chem. Soc.* **134**, 16476–16479 (2012).
13. H. A. Gasteiger, S. S. Kocha, B. Sompalli, F. T. Wagner, *Appl. Catal. B* **56**, 9–35 (2005).
14. J. Suntivich *et al*., *Nat. Chem.* **3**, 647 (2011).
15. I. E. L. Stephens, A. S. Bondarenko, U. Grønbjerg, J. Rossmeisl, I. Chorkendorff, *Energy Environ. Sci.* **5**, 6744–6762 (2012).
16. J. K. Nørskov *et al*., *J. Phys. Chem. B* **108**, 17886–17892 (2004).
17. I. E. L. Stephens *et al*., *J. Am. Chem. Soc.* **133**, 5485–5491 (2011).
18. F. Calle-Vallejo *et al*., *Chem. Sci.* **4**, 1245 (2013).
19. F. Calle-Vallejo, J. I. Martínez, J. M. García-Lastra, E. Abad, M. T. M. Koper, *Surf. Sci.* **607**, 47–53 (2013).
20. J. D. Baran, H. Grönbeck, A. Hellman, *J. Am. Chem. Soc.* **136**, 1320–1326 (2014).
21. H. Li, Y. Li, M. T. M. Koper, F. Calle-Vallejo, *J. Am. Chem. Soc.* **136**, 15694–15701 (2014).
22. F. Calle-Vallejo, M. T. M. Koper, A. S. Bandarenka, *Chem. Soc. Rev.* **42**, 5210–5230 (2013).
23. F. Viñes, J. R. B. Gomes, F. Illas, *Chem. Soc. Rev.* **43**, 4922–4939 (2014).
24. J. Kleis *et al*., *Catal. Lett.* **141**, 1067–1071 (2011).
25. G. Mpourmpakis, A. N. Andriotis, D. G. Vlachos, *Nano Lett.* **10**, 1041–1045 (2010).
26. Materials and methods are available as supplementary materials on *Science* Online.
27. F. Calle-Vallejo, J. I. Martínez, J. M. García-Lastra, P. Sautet, D. Loffreda, *Angew. Chem. Int. Ed.* **53**, 8316–8319 (2014).
28. P. Strasser, S. Koh, J. Greeley, *Phys. Chem. Chem. Phys.* **10**, 3670–3683 (2008).
29. A. A. Topalov *et al*., *Angew. Chem. Int. Ed.* **51**, 12613–12615 (2012).
30. D. C. Johnson, D. T. Napp, S. Bruckenstein, *Electrochim. Acta* **15**, 1493–1509 (1970).
31. B. D. B. Aaronson *et al*., *J. Am. Chem. Soc.* **135**, 3873–3880 (2013).

ACKNOWLEDGMENTS

We received funding from The Netherlands Organisation for Scientific Research (NWO), Veni project 722.014.009; the European Union's FP7/2007-2013 program, grant 303419 (PUMA MIND); the Cluster of Excellence RESOLV (EXC 1069) funded by Deutsche Forschungsgemeinschaft, Helmholtz-Energie-Allianz (HA-E-0002), and SFB 749; and the Cluster of Excellence Nanosystems Initiative Munich. We thank Stichting Nationale Computerfaciliteiten (NCF), Institut du Développement et des Ressources en Informatique Scientifique, Centre Informatique National de l'Enseignement Supérieur (project 609, GENCI/CT8), and Pôle Scientifique de Modélisation Numérique for CPU time. We thank A. Pathan, M. Schmuck, and A. Zychma (RUB) for supporting measurements. The DFT data appear in tables S1 to S3.

SUPPLEMENTARY MATERIALS

www.sciencemag.org/content/350/6257/185/suppl/DC1
Materials and Methods
Figs. S1 to S22
Tables S1 to S3
References (*32*–*40*)

14 April 2015; accepted 2 September 2015
10.1126/science.aab3501

SURFACE CHEMISTRY

Identification of active sites in CO oxidation and water-gas shift over supported Pt catalysts

Kunlun Ding,[1] Ahmet Gulec,[2] Alexis M. Johnson,[1] Neil M. Schweitzer,[3] Galen D. Stucky,[4] Laurence D. Marks,[2] Peter C. Stair[1,5]*

Identification and characterization of catalytic active sites are the prerequisites for an atomic-level understanding of the catalytic mechanism and rational design of high-performance heterogeneous catalysts. Indirect evidence in recent reports suggests that platinum (Pt) single atoms are exceptionally active catalytic sites. We demonstrate that infrared spectroscopy can be a fast and convenient characterization method with which to directly distinguish and quantify Pt single atoms from nanoparticles. In addition, we directly observe that only Pt nanoparticles show activity for carbon monoxide (CO) oxidation and water-gas shift at low temperatures, whereas Pt single atoms behave as spectators. The lack of catalytic activity of Pt single atoms can be partly attributed to the strong binding of CO molecules.

Low-temperature catalytic conversions of carbon monoxide (CO) to carbon dioxide (CO_2) via oxidation and water-gas shift (WGS) reactions are integral to several important processes, including the removal of CO from hydrogen gas (H_2) for fuel cell applications (*1*, *2*) and emission control in automobiles with catalytic converters (*3*). Supported noble metal–based catalysts, mainly platinum (Pt) and gold (Au), have been intensively studied for the reactions during the past decade because of their excellent activity and stability at low reaction temperatures. However, the reaction mechanisms are still highly debated, especially regarding the active site structures—single atoms (*4*–*10*) versus small Pt and Au nanoparticles (NPs) (*11*–*16*). For instance, there have been disagreements on the promotional effects of alkali cations in CO oxidation (*17*–*20*) and WGS (*5*, *10*, *16*, *21*) reactions over supported Pt and Au catalysts. Some researchers attributed the promotional effects to the increased dispersion and activity of Pt and Au single atoms (*5*, *10*); others correlated it to the increased activity of Pt and Au NPs (*16*–*21*). These differences in reaction mechanisms and identification of active sites may have arisen from conclusions drawn from techniques—such as microscopy or x-ray absorption spectroscopy—that provide either statistically limited information or sample-averaged information, respectively. A direct observation of the catalytic performance of specific sites has long been lacking.

Site-specific techniques that provide statistically sufficient information on site identification and quantification as well as the activity evaluation of specific sites would make substantial progress toward resolving these discrepancies. Infrared (IR) spectroscopy of CO on supported noble metal catalysts is widely used because of its sensitivity to the atomic and electronic structures of the binding sites (*22*–*24*). Work done by Green *et al.* on titanium dioxide (TiO_2)–supported Au NPs showed that IR spectroscopy could identify the active site in CO oxidation (*25*) and that CO oxidation occurred within a zone at the perimeter of Au NPs surrounded by a TiO_2 surface. Here, we show that IR spectroscopy with CO as a probe molecule can differentiate and quantify both Pt single atoms and NPs. We confirm the coexistence of Pt single atoms and NPs in many conventional catalysts and show that only the CO molecules adsorbed on Pt NPs can react at low temperatures upon O_2 or H_2O exposure. Thus, the active sites in CO oxidation and WGS reactions are present on the NPs but not on single atoms.

CO molecules were adsorbed on a series of Pt catalysts with varying ratios of Pt single atoms to NPs in order to investigate the corresponding changes to the IR absorption bands. Mesoporous zeolite HZSM-5 [silicon/aluminum (Si/Al) ratio of 62; morphology shown in fig. S1] (*26*) was chosen as the catalyst support because Al atoms are strictly isolated in the zeolite framework (*27*), providing isolated binding sites for Pt. The mesoporous structure is introduced so as to facilitate the diffusion of an organometallic Pt precursor, trimethyl(methylcyclopentadienyl)platinum ($MeCpPtMe_3$), to the Al sites. Pt was loaded on the mesoporous HZSM-5 via either solution grafting at room temperature or vapor deposition at elevated temperatures (*26*).

The IR spectra of adsorbed CO on four Pt/HZSM-5 samples with different loadings (Fig. 1A) reveal two sets of CO absorption bands centered

[1]Department of Chemistry, Northwestern University, Evanston, IL 60208, USA. [2]Department of Materials Science and Engineering, Northwestern University, Evanston, IL 60208, USA. [3]Department of Chemical and Biological Engineering, Northwestern University, Evanston, IL 60208, USA. [4]Department of Chemistry and Biochemistry, University of California, Santa Barbara, CA 93106, USA. [5]Chemical Sciences and Engineering Division, Argonne National Laboratory, Argonne, IL 60439, USA.
***Corresponding author. E-mail: pstair@northwestern.edu**

Editor's Summary

Accounting for surface coordination

The exploration of heterogeneous catalysts using first-principles calculations can be daunting because the large number of atoms and possible surface geometries. Calle-Vallejo *et al.* describe a simpler metric for assessing optimal reactivity: a weighted average of surface coordination that includes second-nearest neighbors (see the Perspective by Stephens *et al.*). The calculations identified three approaches for introducing cavity sites into the platinum(111) surface to improve its performance for the oxygen reduction reaction used in fuel cells.

Science, this issue p. 185, see also p. 164